

Received 8 November 2022; revised 12 December 2022 and 30 December 2022; accepted 23 January 2023. Date of publication 22 February 2023; date of current version 22 May 2023. The review of this paper was arranged by Editor Sergio Fantini.

Digital Object Identifier 10.1109/OJEMB.2023.3246929

# Single Source-Detector Separation Approach to Calculate Tissue Oxygen Saturation Using Continuous Wave Near-Infrared Spectroscopy

THIEN NGUYEN , SOONGHO PARK , BRIAN HILL, AND AMIR H. GANDJBAKHCHE 

Eunice Kennedy Shriver National Institute of Child Health and Human Development, National Institutes of Health, Bethesda, MD 20892 USA

CORRESPONDING AUTHOR: AMIR H. GANDJBAKHCHE (e-mail: gandjbaa@mail.nih.gov)

**ABSTRACT** Currently, common optical techniques to measure tissue oxygen saturation (StO<sub>2</sub>) include time domain (TD), frequency domain (FD), and continuous wave (CW) near-infrared spectroscopy (NIRS). While TD- and FD-NIRS can provide absolute hemoglobin concentration, these systems are often complex and expensive. CW-NIRS, such as diffuse reflectance spectroscopy and spatially resolved spectroscopy (SRS), are simpler and more affordable, but they still require at least two source-detector separations. Here, we propose a single source-detector separation (SSDS) approach to measure StO<sub>2</sub> using reflected intensities from three wavelengths. The accuracy of the SSDS-based StO<sub>2</sub> measurement was verified using an optical simulation and an in-vivo experiment. Simulated spatially dependent reflectance was generated using the Virtual Tissue Simulator on a 1-layer model, which has StO<sub>2</sub> ranging from 0% to 100%. SSDS calculation yielded an equivalent StO<sub>2</sub> to the actual value (average error = 0.3% ± 0.5%). We then performed StO<sub>2</sub> measurements on seven healthy volunteers in the prefrontal cortex during a simulated hypercapnia test using a CW-NIRS device. This device consists of a light source and two photodetectors, which are 30 mm and 40 mm away from the light source. The cerebral oxygen saturation was calculated using both the SRS approach, which uses the reflected intensities at both separations, and the SSDS approach, which employs the reflected intensities at either 30 mm or 40 mm separation. The SRS-based StO<sub>2</sub> calculation was similar to the value calculated from the SSDS method (average difference = 5.0% ± 1.1%). This proposed method will help to advance the development of miniaturized technologies to monitor StO<sub>2</sub> continuously.

**INDEX TERMS** Near-infrared spectroscopy, StO<sub>2</sub>, multiwavelength, wearable, in-vivo.

**IMPACT STATEMENT** A novel avenue to measure tissue oxygen saturation noninvasively with high accuracy using a multiwavelength LED and a photodetector was developed and verified with an optical simulation and in-vivo experiment.

## I. INTRODUCTION

**T**ISSUE oxygen saturation (StO<sub>2</sub>) is an important parameter to assess oxygen delivery and uptake in tissue. Hypoxia, a term to indicate inadequate StO<sub>2</sub>, is often seen in patients with cardiac problems, respiratory infections, or pulmonary diseases [1], [2], [3], [4], [5]. Prolonged hypoxia can damage vital organs such as the brain, lungs, and heart, and can tragically lead to death. Due to its critical role in maintaining organ function, StO<sub>2</sub> has been frequently used to monitor patient health. Common sites to measure StO<sub>2</sub>

include the brain [6], spinal cord [7], [8], peripheral muscle [9], leg [10], kidney [11], [12], and placenta [13].

Current techniques to evaluate the oxygenation level in a tissue include invasive methods, such as Clark-type electrodes [14], electron spin resonance probes [15], and fiber optic probes with phosphorescent dyes [16], and non-invasive methods, such as magnetic resonance imaging (MRI) [17], positron emission tomography (PET) [18], and near-infrared spectroscopy (NIRS) [6], [13], [19]. While invasive methods provide a direct measurement of the oxygenation level with

This work is licensed under a Creative Commons Attribution 4.0 License. For more information, see <http://creativecommons.org/licenses/by/4.0/>

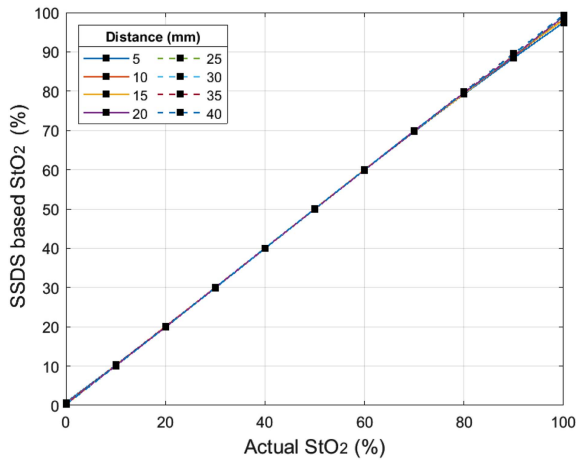


**FIGURE 1.** Comparison between actual and calculated  $\text{StO}_2$  in an optical simulation when DPF values were specified. Different line colors and patterns represent  $\text{StO}_2$  calculated from different separations.

high accuracy, they are more resource intensive and may create new pathways for infections [20]. Additionally, psychologically, most patients are reluctant to undergo invasive tests. For these reasons, non-invasive methods are often preferable. However, MRI and PET have disadvantages of limited observation sites and difficult continuous monitoring due to the use of bulky and expensive equipment. In addition, PET requires injecting a tracer such as a radioisotope ‘Oxygen-15’ into the patient’s body. NIRS is a compact system that can non-invasively measure  $\text{StO}_2$ . There are three main types of NIRS: time domain (TD), frequency domain (FD), and continuous wave (CW) NIRS [6], [13], [19]. While TD- and FD-NIRS can provide absolute hemoglobin concentration, these systems are often complex. CW-NIRS, such as diffuse reflectance spectroscopy (DRS) and spatially resolved spectroscopy (SRS), can be made simpler, wearable, and affordable, but they still require at least two source-detector separations.

In this study, we propose a single source-detector separation (SSDS) method to measure  $\text{StO}_2$ . The SSDS approach was developed based on the previously reported relationship between the attenuation difference of a selected wavelength pair and the proportion of oxy- and met-myoglobin in meat tissue [21], [22], [23]. The main absorbance of meat tissue is myoglobin, whereas the dominant absorbance of in-vivo human tissues is hemoglobin, however, hemoglobin has a similar spectral extinction with myoglobin. Therefore, we hypothesize that it is possible to use the attenuation differences from certain wavelength pairs to compute the proportion of oxy-hemoglobin (HbO) in an in-vivo human tissue, which is equivalent to  $\text{StO}_2$ . The advantage of this approach lies in its simplicity thanks to the need for only one source-detector separation, which will greatly benefit miniaturized technologies.

## II. RESULTS

### A. SIMULATED TISSUE OXYGEN SATURATION

Simulated reflectance intensities from each source-detector separation were used to calculate  $\text{StO}_2$ . Fig. 1 represents

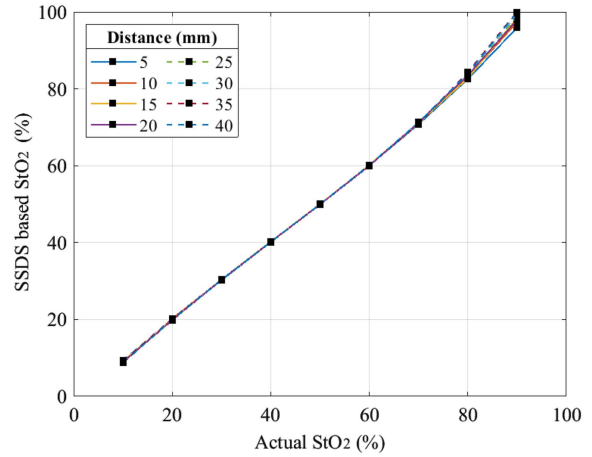


**FIGURE 2.** Comparison between actual and calculated  $\text{StO}_2$  in an optical simulation when DPF at 730, 800, and 850 nm is assumed to be the same. Different line colors and patterns represent  $\text{StO}_2$  calculated from different separations.

the actual  $\text{StO}_2$  and the calculated  $\text{StO}_2$  based on the SSDS approach using an estimated differential pathlength factor (DPF) at each wavelength and saturation level. The actual  $\text{StO}_2$  and the calculated value are equivalent across all source-detector separations with an averaged error of  $0.3\% \pm 0.5\%$  (Fig. 1). The error was calculated as the absolute difference between the calculated and the actual  $\text{StO}_2$ . The average errors across all separations are small in the 10% to 70%  $\text{StO}_2$  range (errors  $< 0.2\%$ ). However, the errors are larger at 0% and 80% to 100%  $\text{StO}_2$  (errors  $> 0.3\%$ , at 100%, the average error = 1.4%).

When the DPF values at the three selected wavelengths were assumed to be the same, the SSDS-based  $\text{StO}_2$  calculation resulted in a negative saturation at 0%  $\text{StO}_2$  and more than 100% at 100%  $\text{StO}_2$ . Hence, comparison between the SSDS-based  $\text{StO}_2$  and the actual value was only performed in the 10% to 90% saturation range (Fig. 2). In this range, the average error across separations is  $1.7\% \pm 2.7\%$ . Similar to the previous case, the errors are small in the 10% to 70%  $\text{StO}_2$  range (errors  $\leq 1.1\%$ ). However, the errors are greater at 80% (error = 3.5%) and 90% (error = 8.5%)  $\text{StO}_2$ .

### B. CEREBRAL OXYGEN SATURATION DURING A SIMULATED HYPERCAPNIA TEST

Fig. 3 shows cerebral oxygen saturation calculated from the conventional SRS method and the proposed SSDS method in the prefrontal cortex during a simulated hypercapnia test in a representative participant (subject 3). Since the SSDS method needs only one source-detector separation to calculate oxygen saturation, two separate value sets from the 30 mm and 40 mm separations were derived. The  $\text{StO}_2$  calculated from both the SRS and SSDS methods follows the same response trend with a sharp increase during the intervention and a quick return to baseline during a resting state. In comparison to the  $\text{StO}_2$  calculated from the 40 mm SSDS, the  $\text{StO}_2$  calculated from the 30 mm SSDS appears to be closer to the value calculated from the SRS method (Fig. 3).

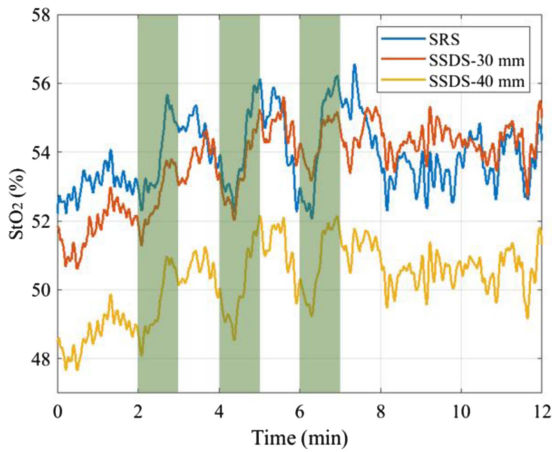


**FIGURE 3.** Cerebral oxygen saturation during a simulated hypercapnia test from subject 3. Green shades indicate the timelines when a participant was under a hypercapnia intervention.

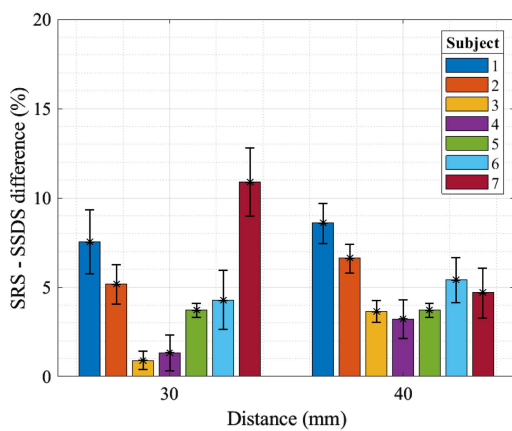


**FIGURE 4.** Difference between the  $StO_2$  calculated from the conventional SRS method and the proposed SSDS method.

**C. DIFFERENCE AND CORRELATION**

A saturation difference was calculated by taking the absolute difference between the SRS-based  $StO_2$  and the SSDS-based  $StO_2$  at each time point. The saturation difference between SRS and 30 mm and 40 mm separations SSDS are relatively small with average differences of  $4.8\% \pm 1.2\%$  and  $5.1\% \pm 1.0\%$ , respectively (Fig. 4). A paired, two-tailed *t*-test across all subjects results in no statistical significance between the SRS – 30 mm SSDS difference and the SRS – 40 mm SSDS difference (*p*-value = 0.8). The saturation differences in subjects 3 and 4 are negligible (as low as 0.9% in subject 3). However, for other participants, the differences are relatively high (as high as 10.9% in subject 7).

The average correlation coefficient between the  $StO_2$  calculated from the SSDS method and the value calculated from the conventional SRS method across participants is  $0.70 \pm 0.15$  (Fig. 5). A paired, two-tailed *t*-test on the correlation coefficients across all subjects results in a significantly higher correlation between the SRS-based  $StO_2$  and the 40 mm SSDS-based  $StO_2$  ( $0.80 \pm 0.08$ ) in comparison to the 30 mm SSDS-based  $StO_2$  ( $0.60 \pm 0.16$ ) (*p*-value < 0.001).

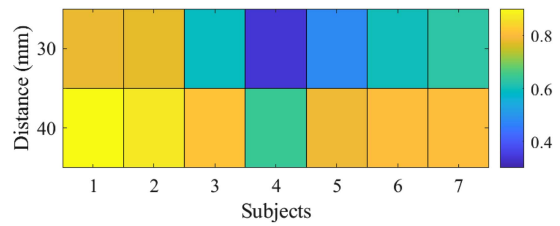


**FIGURE 5.** Correlation between the  $StO_2$  calculated from the conventional SRS method and the proposed SSDS method.

**III. DISCUSSION**

In this study, we derived a model to calculate tissue oxygen saturation using the reflected intensities at three wavelengths 730, 800, and 850 nm from a single source-detector separation. We demonstrated the capability of this model in measuring tissue oxygen saturation in an optical simulation with high accuracy (average error =  $0.3\% \pm 0.5\%$ ). The SSDS-based  $StO_2$  calculation was also proved to be robust over a wide range of source-detector separations. This model was then applied to measure the cerebral oxygen saturation in the prefrontal cortex during a simulated hypercapnia test. The  $StO_2$  calculated from the proposed SSDS model was similar to the value calculated from the conventional SRS method (average difference =  $5.0\% \pm 1.1\%$  and average correlation =  $0.70 \pm 0.15$ ). The advantage of the SSDS, which is the need for only a single source-detector separation, will help simplify the circuit design, lower the manufacturing cost, and miniaturize the size of a tissue oximeter.

The discrepancy (5.0% average difference) between the saturation calculated using the SSDS and the SRS methods is believed to arise from the geometry of the head and different signals used to calculate the  $StO_2$ . While the SSDS method use the reflected light intensities from either 30 mm or 40 mm separation, the SRS method uses the signals from both separations. Additionally, the human head is comprised of multiple tissue layers (scalp, skull, epidural membrane, and cerebral cortex), which have different optical properties and possibly different oxygen saturation. Therefore, the two methods may measure  $StO_2$  from different sampled volume. In order to verify the sampled volume of each method, future studies should perform simulation on multiple-layer tissue. There exists a bias among participants in the difference between  $StO_2$  calculated from the two methods. While the differences are negligible in subjects 3 and 4, they are higher in other subjects. The bias could come from the individual differences in the thicknesses of the head tissues and the oxygen saturation of each tissue type. To further understanding the bias, various thicknesses and oxygen saturation of each tissue layer should be included in the future simulations.

The initial equation, which was used to develop the SSDS approach, is the modified Beer-Lamberts’ law. The modified law contains an unknown factor, which making it not possible to calculate the absolute concentration of hemoglobin. Instead, it is often applied to compute the changes in oxy- and deoxy-hemoglobin concentration in a tissue. Previously, Sassaroli and Fantini reported that the form of the modified

Beer-Lamberts' law used in this study is not strictly correct [24]. However, in this work, we have retained this form because we are specifically targeting StO<sub>2</sub>, which is a rather robust parameter even under strong approximations of the model used. Hence, it is likely that the SSDS approach is valid. Specifically, the high accuracy of StO<sub>2</sub> calculation from the simulation (error = 0.3%) has proved the validity of the SSDS approach.

To develop the equation to calculate tissue oxygen separation using reflected intensities at multiple wavelengths (10), which was derived from the "Equation Derivation" section, we have made two assumptions. The first assumption was that the unknown geometry dependent factors at 2 selected wavelengths are equal ( $G_1 = G_2$ ). This assumption is not strictly correct, however, the simulation results obtained in the semi-infinite medium geometry have proven that this assumption may not be critical. The second assumption was that the hemoglobin in a tissue exists in only oxy- and deoxy-hemoglobin forms. This assumption is generally true in a normal and healthy individual. However, in patients with methemoglobinemia, there will be elevated met-hemoglobin in the patients' blood. In this case, met-hemoglobin should be taken into account.

#### IV. CONCLUSION

This study proposes a novel avenue of using reflected intensities at three wavelengths from a single source-detector separation to calculate tissue oxygen saturation. A model relating tissue oxygen saturation with intensities collected from three wavelengths was derived. This model was tested with an optical simulation and demonstrated high accuracy in computing tissue oxygen saturation. In addition, the cerebral oxygen saturation in the prefrontal cortex calculated from the single source-detector separation method has high similarity and correlation with the value calculated from the conventional spatially resolved spectroscopy technique. This suggested method can help to simplify a tissue oximeter.

#### V. MATERIALS AND METHODS

##### A. EQUATION DERIVATION

To derive an equation to compute StO<sub>2</sub> using reflected intensities at multiple wavelengths, we started with the modified

Beer-Lamberts' law.

$$\text{Attenuation (OD)} = -\log(I/I^0) = \langle DPF \rangle \cdot \mu_a \cdot d_p + G \quad (1)$$

where  $I$  is the light intensity detected at a detector,  $I^0$  is the light intensity emitted by the source,  $\langle DPF \rangle = \frac{1}{\mu_a} \int_0^{\mu_a} DPF \cdot \mu'_a d\mu'_a$  where  $DPF$  is the differential pathlength factor,  $\mu_a$  is the absorption coefficient of the interested tissue,  $d_p$  is the source-detector separation, and  $G$  is an unknown geometry dependent factor.

At a specific wavelength, (1) for a tissue which contains oxy- and deoxy- hemoglobin (HbO, Hb) becomes:

$$OD(\lambda_1) = d \cdot \langle DPF \rangle_1 \cdot \left( \varepsilon_{\lambda_1}^{HbO} \cdot c_{HbO} + \varepsilon_{\lambda_1}^{Hb} \cdot c_{Hb} \right) + G_1 \quad (2)$$

Where  $OD$  is the attenuation,  $\varepsilon_{\lambda_1}^{HbO}$  is the extinction coefficient of HbO at wavelength  $\lambda_1$ , and  $c_{HbO}$  is the concentration of HbO.

By replacing the concentration with the proportion, (2) is:

$$OD(\lambda_1) = d \cdot \langle DPF \rangle_1 \cdot \left( \varepsilon_{\lambda_1}^{HbO} \cdot p_{HbO} \cdot c_{total} + \varepsilon_{\lambda_1}^{Hb} \cdot p_{Hb} \cdot c_{total} \right) + G_1 \quad (3)$$

where  $p_{HbO}$  is the proportion of HbO,  $c_{total}$  is the total concentration of hemoglobin, and  $c_{HbO} = p_{HbO} \cdot c_{total}$ .

Similarly, (3) can be replicated at another wavelength  $\lambda_2$ :

$$OD(\lambda_2) = d \cdot \langle DPF \rangle_2 \cdot \left( \varepsilon_{\lambda_2}^{HbO} \cdot p_{HbO} \cdot c_{total} + \varepsilon_{\lambda_2}^{Hb} \cdot p_{Hb} \cdot c_{total} \right) + G_2 \quad (4)$$

With an assumption that  $G_1 = G_2$ , by subtracting both sides of (3) to (4), we have:

$$OD(\lambda_1) - OD(\lambda_2) = d \cdot c_{total} \cdot \left\{ \langle DPF \rangle_1 \cdot \left( \varepsilon_{\lambda_1}^{HbO} \cdot p_{HbO} + \varepsilon_{\lambda_1}^{Hb} \cdot p_{Hb} \right) - \langle DPF \rangle_2 \cdot \left( \varepsilon_{\lambda_2}^{HbO} \cdot p_{HbO} + \varepsilon_{\lambda_2}^{Hb} \cdot p_{Hb} \right) \right\} \quad (5)$$

By replacing  $\lambda_3$  to  $\lambda_1$ , (5) becomes:

$$OD(\lambda_3) - OD(\lambda_2) = d \cdot c_{total} \cdot \left\{ \langle DPF \rangle_3 \cdot \left( \varepsilon_{\lambda_3}^{HbO} \cdot p_{HbO} + \varepsilon_{\lambda_3}^{Hb} \cdot p_{Hb} \right) - \langle DPF \rangle_2 \cdot \left( \varepsilon_{\lambda_2}^{HbO} \cdot p_{HbO} + \varepsilon_{\lambda_2}^{Hb} \cdot p_{Hb} \right) \right\} \quad (6)$$

When dividing both sides of (5) to (6), we have (7), shown at the bottom of the page.

$$\frac{OD(\lambda_1) - OD(\lambda_2)}{OD(\lambda_3) - OD(\lambda_2)} = \frac{\langle DPF \rangle_1 \cdot \left( \varepsilon_{\lambda_1}^{HbO} \cdot p_{HbO} + \varepsilon_{\lambda_1}^{Hb} \cdot p_{Hb} \right) - \langle DPF \rangle_2 \cdot \left( \varepsilon_{\lambda_2}^{HbO} \cdot p_{HbO} + \varepsilon_{\lambda_2}^{Hb} \cdot p_{Hb} \right)}{\langle DPF \rangle_3 \cdot \left( \varepsilon_{\lambda_3}^{HbO} \cdot p_{HbO} + \varepsilon_{\lambda_3}^{Hb} \cdot p_{Hb} \right) - \langle DPF \rangle_2 \cdot \left( \varepsilon_{\lambda_2}^{HbO} \cdot p_{HbO} + \varepsilon_{\lambda_2}^{Hb} \cdot p_{Hb} \right)} \quad (7)$$

$$\frac{\log(k_1 \cdot I_{\lambda_2}/I_{\lambda_1})}{\log(k_2 \cdot I_{\lambda_2}/I_{\lambda_3})} = \frac{\langle DPF \rangle_1 \cdot \left( \varepsilon_{\lambda_1}^{HbO} \cdot p_{HbO} + \varepsilon_{\lambda_1}^{Hb} \cdot p_{Hb} \right) - \langle DPF \rangle_2 \cdot \left( \varepsilon_{\lambda_2}^{HbO} \cdot p_{HbO} + \varepsilon_{\lambda_2}^{Hb} \cdot p_{Hb} \right)}{\langle DPF \rangle_3 \cdot \left( \varepsilon_{\lambda_3}^{HbO} \cdot p_{HbO} + \varepsilon_{\lambda_3}^{Hb} \cdot p_{Hb} \right) - \langle DPF \rangle_2 \cdot \left( \varepsilon_{\lambda_2}^{HbO} \cdot p_{HbO} + \varepsilon_{\lambda_2}^{Hb} \cdot p_{Hb} \right)} \quad (8)$$

$$\frac{\log(k_1 \cdot I_{\lambda_2}/I_{\lambda_1})}{\log(k_2 \cdot I_{\lambda_2}/I_{\lambda_3})} = \frac{StO_2 \cdot \left\{ \langle DPF \rangle_1 \cdot \left( \varepsilon_{\lambda_1}^{HbO} - \varepsilon_{\lambda_1}^{Hb} \right) - \langle DPF \rangle_2 \cdot \left( \varepsilon_{\lambda_2}^{HbO} - \varepsilon_{\lambda_2}^{Hb} \right) \right\} + \langle DPF \rangle_1 \cdot \varepsilon_{\lambda_1}^{Hb} - \langle DPF \rangle_2 \cdot \varepsilon_{\lambda_2}^{Hb}}{StO_2 \cdot \left\{ \langle DPF \rangle_3 \cdot \left( \varepsilon_{\lambda_3}^{HbO} - \varepsilon_{\lambda_3}^{Hb} \right) - \langle DPF \rangle_2 \cdot \left( \varepsilon_{\lambda_2}^{HbO} - \varepsilon_{\lambda_2}^{Hb} \right) \right\} + \langle DPF \rangle_3 \cdot \varepsilon_{\lambda_3}^{Hb} - \langle DPF \rangle_2 \cdot \varepsilon_{\lambda_2}^{Hb}} \quad (9)$$

**TABLE I** Extinction Coefficients of HbO and Hb at Selected Wavelengths

Hemoglobin	730 nm (cm <sup>-1</sup> /moles/L)	800 nm (cm <sup>-1</sup> /moles/L)	850 nm (cm <sup>-1</sup> /moles/L)
HbO	510	863.3	1097
Hb	1296.5	838.7	781

Since  $OD = -\log(I/I^0) = \log(I^0/I)$ , the difference in the optical intensities at two wavelengths can be calculated in term of the reflected intensities at these wavelengths as: where  $I_{\lambda_1}^0 = k_1 \cdot I_{\lambda_2}^0$ . Similarly,  $OD(\lambda_3) - OD(\lambda_2) = \log(k_2 \cdot I_{\lambda_2}/I_{\lambda_3})$ , where  $I_{\lambda_3}^0 = k_2 \cdot I_{\lambda_2}^0$ .

Hence, (7) becomes (8), shown at the bottom of the previous page.

Here, we assume that hemoglobin in a tissue mostly exists in either oxy-hemoglobin or deoxy-hemoglobin forms, which means  $p_{HbO} + p_{Hb} = 1$ . On the other hand, we have  $StO_2 = \frac{p_{HbO}}{p_{HbO} + p_{Hb}} = p_{HbO}$ . Hence, by substituting  $StO_2$  for  $p_{HbO}$ , and  $1 - StO_2$  for  $p_{Hb}$ , (8) will be as in (9), shown at the bottom of the previous page.

By rearranging (9), we can obtain (10), shown at the bottom of the page, which can be used to calculate  $StO_2$ .

### B. OXYGENATION CALCULATION USING INTENSITIES AT THREE WAVELENGTHS

To solve (10), the extinction coefficients of the two hemoglobin species and the differential pathlength factors (DPF) at three wavelengths are needed. For the application of the method, we have used DPF at the end of the range (0,  $\mu_a$ ), which is  $DPF(\mu_a)$ . Depending on the selected wavelengths and interested tissues, DPF can be available [25], [26], [27]. In this study, we selected three wavelengths at 730, 800, and 850 nm. The extinction coefficients of these three wavelengths are provided in Table I [28].

### C. SIMULATION ON A SEMI-INFINITE MEDIUM GEOMETRY

The accuracy of the SSDS measurement was first tested using an optical simulation at three wavelengths: 730, 800, and 850 nm. Simulated spatially dependent reflectance results were generated using the Virtual Tissue Simulator (VTS) NURBS scaled Monte Carlo for semi-infinite medium geometry [29]. The simulated medium had a reduced scattering coefficient ( $\mu'_s$ ) of 1 mm<sup>-1</sup> and varied absorption coefficients ( $\mu_a$ ) (Table II) based on the oxygen saturation level. The absorption coefficients at the three wavelengths were calculated based on a fixed total hemoglobin concentration of 100  $\mu\text{mol}$

**TABLE II** Absorption Coefficients Used to Perform Simulation

Actual oxygenation level (%)	730 nm (mm <sup>-1</sup> )	800 nm (mm <sup>-1</sup> )	850 nm (mm <sup>-1</sup> )
0	0.029244	0.018918	0.017617
10	0.02747	0.018974	0.018329
20	0.025696	0.019029	0.019042
30	0.023922	0.019085	0.019755
40	0.022148	0.01914	0.020468
50	0.020374	0.019195	0.02118
60	0.0186	0.019251	0.021893
70	0.016826	0.019306	0.022606
80	0.015052	0.019362	0.023319
90	0.013278	0.019417	0.024032
100	0.011504	0.019473	0.024744

and oxygen saturation ranging from 0% to 100% (Table II). Simulations were performed at 8 source-detector separations, ranging from 5 mm to 40 mm. The reflected intensities at each separation were then fed to (10) to compute  $StO_2$  with  $k_1 = k_2 = 1$ . The  $StO_2$  calculation was performed in two cases, when DPF at the three wavelengths were assumed to be the same ( $DPF_1 = DPF_2 = DPF_3$ ) and when a specific DPF value was calculated for each wavelength at each saturation using (11). (11) is an approximated version of the one reported in the literature under the zero-boundary condition [30].

$$DPF = \frac{1}{2} \left( \frac{3\mu'_s(\lambda)}{\mu_a(\lambda)} \right)^{1/2} \quad (11)$$

where  $\mu'_s = 1 \text{ mm}^{-1}$  and  $\mu_a$  is in Table II.

### D. IN-VIVO EXPERIMENT

In-vivo  $StO_2$  measurements were performed on seven adult healthy volunteers (5 females, aged  $42.7 \pm 13.7$  years old) during a simulated hypercapnia test. The study procedures followed the guidelines and regulations described in a protocol approved by the National Institute of Child Health and Human Development (NICHD) Institutional Review Board (21CH0028). This study relied on subjects recruited as part of a clinical trial, which can be found at the <https://clinicaltrials.gov/> (A Noninvasive Multimodal Biosensing Device for Screening and Monitoring Response to Treatment of Infectious Respiratory Diseases, NCT05035420). Prior to a measurement, a CW-NIRS device (prototype provided by Hamamatsu photonics K.K., Japan) [31] was placed on the

$StO_2 =$

$$\frac{\langle DPF \rangle_3 \cdot \log(k_1 \cdot I_{\lambda_2}/I_{\lambda_1}) \cdot \varepsilon_{\lambda_3}^{Hb} - \langle DPF \rangle_1 \cdot \log(k_2 \cdot I_{\lambda_2}/I_{\lambda_3}) \cdot \varepsilon_{\lambda_1}^{Hb} + \langle DPF \rangle_2 \cdot \log(k_2 \cdot I_{\lambda_1}/k_1 \cdot I_{\lambda_3}) \cdot \varepsilon_{\lambda_2}^{Hb}}{\langle DPF \rangle_1 \cdot \log(k_2 \cdot I_{\lambda_2}/I_{\lambda_3}) \left( \varepsilon_{\lambda_1}^{HbO} - \varepsilon_{\lambda_1}^{Hb} \right) - \langle DPF \rangle_3 \cdot \log(k_1 \cdot I_{\lambda_2}/I_{\lambda_1}) \left( \varepsilon_{\lambda_3}^{HbO} - \varepsilon_{\lambda_3}^{Hb} \right) + \langle DPF \rangle_2 \cdot \log(k_1 \cdot I_{\lambda_3}/k_2 \cdot I_{\lambda_1}) \left( \varepsilon_{\lambda_2}^{HbO} - \varepsilon_{\lambda_2}^{Hb} \right)} \quad (10)$$

participant's forehead. During the measurement, the participant wore a two-way non-rebreathing facemask (Hans Rudolph, Inc., Kansas), which covered his/her nose and mouth. The mask's inflow port was connected to a Douglas bag (Harvard Bioscience, Inc., Holliston) through a smooth bore tubing (AFT7, Biopac Systems, Inc., California) and a 3-way valve (Hans Rudolph, Inc., Kansas), and its outflow port was open to the room air. The Douglas bag contained a mixture of 5% carbon dioxide and 95% normal air. The participant first breathed normal air for 2 minutes, then switched between hypercapnia intervention and normal air every 1 minute for 6 minutes, and finally breathed normal air for 4 minutes. The total experiment time was 12 minutes. The CW-NIRS device consists of a multiwavelength (730, 800, and 850 nm) LED and two photodetectors. The photodetectors were placed 30 mm and 40 mm away from the LED.  $StO_2$  was calculated using both the SRS approach, which uses reflected intensities at both 30 mm and 40 mm separations (19), and the SSDS approach, which employs reflected intensities at either separation. Reflected intensities at either 30 mm or 40 mm separation were fed to (10) to calculate  $StO_2$  with  $k_1 = k_2 = 1$  and an assumption of equal DPF at three wavelengths ( $DPF_1 = DPF_2 = DPF_3$ ).

#### ACKNOWLEDGMENT

We acknowledge open-source software resources offered by the Virtual Photonics Technology Initiative (<https://virtualphotonics.org>), at the Beckman Laser Institute, University of California, Irvine. We would like to send special thanks to Hamamatsu Photonics company for lending us their prototype to conduct in-vivo experiments. We would like to thank the intramural research program at the Eunice Kennedy Shriver National Institute of Child Health and Human Development for supporting us to perform this research.

#### REFERENCES

- [1] R. Samsel and P. Schumacker, "Oxygen delivery to tissues," *Eur. Respir. J.*, vol. 4, no. 10, pp. 1258–1267, 1991.
- [2] D. Green and G. Kunst, "Cerebral oximetry and its role in adult cardiac, non-cardiac surgery and resuscitation from cardiac arrest," *Anaesthesia*, vol. 72, pp. 48–57, Jan. 2017.
- [3] M. R. Geier and D. A. Geier, "Respiratory conditions in coronavirus disease 2019 (COVID-19): Important considerations regarding novel treatment strategies to reduce mortality," *Med. Hypotheses*, vol. 140, 2020, Art. no. 109760.
- [4] R. M. Tuder, J. H. Yun, A. Bhunia, and I. Fijalkowska, "Hypoxia and chronic lung disease," *J. Mol. Med.*, vol. 85, no. 12, pp. 1317–1324, 2007.
- [5] A. Nathan and M. Singer, "The oxygen trail: Tissue oxygenation," *Brit. Med. Bull.*, vol. 55, no. 1, pp. 96–108, 1999.
- [6] J. M. Murkin and M. Arango, "Near-infrared spectroscopy as an index of brain and tissue oxygenation," *Brit. J. Anaesth.*, vol. 103, no. 1, pp. i3–i13, 2009.
- [7] B. Shadgan et al., "Optical assessment of spinal cord tissue oxygenation using a miniaturized near infrared spectroscopy sensor," *J. Neurotrauma*, vol. 36, no. 21, pp. 3034–3043, 2019.
- [8] S. A. LeMaire et al., "Transcutaneous near-infrared spectroscopy for detection of regional spinal ischemia during intercostal artery ligation: Preliminary experimental results," *J. Thoracic Cardiovasc. Surg.*, vol. 132, no. 5, pp. 1150–1155, 2006.
- [9] R. P. Boezeman, F. L. Moll, Ç. Ünlü, and J.-P. P. de Vries, "Systematic review of clinical applications of monitoring muscle tissue oxygenation with near-infrared spectroscopy in vascular disease," *Microvascular Res.*, vol. 104, pp. 11–22, 2016.
- [10] J. J. van Lieshout, F. Pott, P. L. Madsen, J. van Goudoever, and N. H. Secher, "Muscle tensing during standing: Effects on cerebral tissue oxygenation and cerebral artery blood velocity," *Stroke*, vol. 32, no. 7, pp. 1546–1551, 2001.
- [11] P. Hansell, W. J. Welch, R. C. Blantz, and F. Palm, "Determinants of kidney oxygen consumption and their relationship to tissue oxygen tension in diabetes and hypertension," *Clin. Exp. Pharmacol. Physiol.*, vol. 40, no. 2, pp. 123–137, 2013.
- [12] R. G. Evans et al., "Haemodynamic influences on kidney oxygenation: Clinical implications of integrative physiology," *Clin. Exp. Pharmacol. Physiol.*, vol. 40, no. 2, pp. 106–122, 2013.
- [13] T. Nguyen et al., "Non-invasive transabdominal measurement of placental oxygenation: A step toward continuous monitoring," *Biomed. Opt. Exp.*, vol. 12, no. 7, pp. 4119–4130, 2021.
- [14] L. C. Clark Jr., R. Wolf, D. Granger, and Z. Taylor, "Continuous recording of blood oxygen tensions by polarography," *J. Appl. Physiol.*, vol. 6, no. 3, pp. 189–193, 1953.
- [15] B. B. Williams et al., "Clinical electron paramagnetic resonance (EPR) oximetry using India ink," in *Oxygen Transport to Tissue XXXI*, Berlin, Germany: Springer, 2010, pp. 149–156.
- [16] R. I. Dmitriev and D. B. Papkovsky, "Optical probes and techniques for O<sub>2</sub> measurement in live cells and tissue," *Cellular Mol. Life Sci.*, vol. 69, no. 12, pp. 2025–2039, 2012.
- [17] D. Morozov, J. D. Quirk, and S. C. Beeman, "Toward noninvasive quantification of adipose tissue oxygenation with MRI," *Int. J. Obesity*, vol. 44, no. 8, pp. 1776–1783, 2020.
- [18] J. D. Chapman, R. F. Schneider, J.-L. Urbain, and G. E. Hanks, "Single-photon emission computed tomography and positron-emission tomography assays for tissue oxygenation," in *Seminars Radiat. Oncol.*, vol. 11, pp. 47–57, Jan. 2001.
- [19] S. Suzuki, S. Takasaki, T. Ozaki, and Y. Kobayashi, "Tissue oxygenation monitor using NIR spatially resolved spectroscopy," in *Optical Tomography and Spectroscopy of Tissue III*, vol. 3597. Bellingham, WA, USA: SPIE, 1999, pp. 582–592.
- [20] B. Huppertz, "Traditional and new routes of trophoblast invasion and their implications for pregnancy diseases," *Int. J. Mol. Sci.*, vol. 21, no. 1, 2019, Art. no. 289.
- [21] T. Nguyen, K. N. Phan, J.-B. Lee, and J. G. Kim, "Metmyoglobin formation, accumulation, degradation, and myoglobin oxygenation monitoring based on multiwavelength attenuation measurement in porcine meat," *J. Biomed. Opt.*, vol. 21, no. 5, 2016, Art. no. 057002.
- [22] T. Nguyen, S. Kim, and J. G. Kim, "Diffuse reflectance spectroscopy to quantify the met-myoglobin proportion and meat oxygenation inside of pork and beef," *Food Chem.*, vol. 275, pp. 369–376, 2019.
- [23] T. Nguyen and J. G. Kim, "A simple but quantitative method for non-destructive monitoring of myoglobin redox forms inside the meat," *J. Food Sci. Technol.*, vol. 56, no. 12, pp. 5354–5361, 2019.
- [24] A. Sassaroli and S. Fantini, "Comment on the modified Beer–Lambert law for scattering media," *Phys. Med. Biol.*, vol. 49, no. 14, 2004, Art. no. N255.
- [25] M. Hiraoka et al., "A Monte Carlo investigation of optical pathlength in inhomogeneous tissue and its application to near-infrared spectroscopy," *Phys. Med. Biol.*, vol. 38, no. 12, 1993, Art. no. 1859.
- [26] T. Talukdar, S. G. Diamond, and J. H. Moore, "Continuous correction of differential path length factor in near-infrared spectroscopy," *J. Biomed. Opt.*, vol. 18, no. 5, 2013, Art. no. 056001.
- [27] F. Scholkmann and M. Wolf, "General equation for the differential pathlength factor of the frontal human head depending on wavelength and age," *J. Biomed. Opt.*, vol. 18, no. 10, 2013, Art. no. 105004.
- [28] W. Zijlstra, A. Buursma, and W. Meeuwse-Van der Roest, "Absorption spectra of human fetal and adult oxyhemoglobin, de-oxyhemoglobin, carboxyhemoglobin, and methemoglobin," *Clin. Chem.*, vol. 37, no. 9, pp. 1633–1638, 1991.
- [29] C. K. Hayakawa et al., "MCCL: An open-source software application for Monte Carlo simulations of radiative transport," *J. Biomed. Opt.*, vol. 27, no. 8, 2022, Art. no. 083005.
- [30] S. Fantini et al., "Non-invasive optical monitoring of the newborn piglet brain using continuous-wave and frequency-domain spectroscopy," *Phys. Med. Biol.*, vol. 44, no. 6, 1999, Art. no. 1543.
- [31] T. Watanabe, R. Sekine, T. Mizuno, and M. Miwa, "Development of portable, wireless and smartphone controllable near-infrared spectroscopy system," in *Oxygen Transport to Tissue XXXVIII*. Berlin, Germany: Springer, 2016, pp. 385–392.